

See discussions, stats, and author profiles for this publication at: <https://www.researchgate.net/publication/270288345>

The equilibrium shape of fluid–fluid interfaces: Derivation and a new numerical method for Young’s and Young–Laplace equations

ARTICLE *in* THE JOURNAL OF CHEMICAL PHYSICS · DECEMBER 2014

Impact Factor: 2.95 · DOI: 10.1063/1.4904391 · Source: PubMed

CITATION

1

READS

53

3 AUTHORS:



[Giuseppe Soligno](#)

Utrecht University

4 PUBLICATIONS 22 CITATIONS

[SEE PROFILE](#)



[Marjolein Dijkstra](#)

Utrecht University

234 PUBLICATIONS 6,376 CITATIONS

[SEE PROFILE](#)



[René van Roij](#)

Utrecht University

176 PUBLICATIONS 4,127 CITATIONS

[SEE PROFILE](#)



The equilibrium shape of fluid-fluid interfaces: Derivation and a new numerical method for Young's and Young-Laplace equations

Giuseppe Soligno, Marjolein Dijkstra, and René van Roij

Citation: *The Journal of Chemical Physics* **141**, 244702 (2014); doi: 10.1063/1.4904391

View online: <http://dx.doi.org/10.1063/1.4904391>

View Table of Contents: <http://scitation.aip.org/content/aip/journal/jcp/141/24?ver=pdfcov>

Published by the AIP Publishing

Articles you may be interested in

Instrument and methods for surface dilatational rheology measurements
Rev. Sci. Instrum. **79**, 104102 (2008); 10.1063/1.3000569

Drop shape dynamics of a Newtonian drop in a non-Newtonian matrix during transient and steady shear flow
J. Rheol. **51**, 261 (2007); 10.1122/1.2426973

Derivation of the generalized Young-Laplace equation of curved interfaces in nanoscaled solids
J. Appl. Phys. **100**, 074308 (2006); 10.1063/1.2356094

Thermodynamic derivations of the mechanical equilibrium conditions for fluid surfaces: Young's and Laplace's equations
Am. J. Phys. **73**, 1139 (2005); 10.1119/1.2117127

Young-Laplace equation for liquid crystal interfaces
J. Chem. Phys. **113**, 10820 (2000); 10.1063/1.1324993



SUBSCRIBE TO
physics
today

The equilibrium shape of fluid-fluid interfaces: Derivation and a new numerical method for Young's and Young-Laplace equations

Giuseppe Soligno,¹ Marjolein Dijkstra,² and René van Roij¹

¹Institute for Theoretical Physics, Center for Extreme Matter and Emergent Phenomena, Utrecht University, Leuvenlaan 4, Utrecht 3584 CE, The Netherlands

²Soft Condensed Matter, Debye Institute for Nanomaterials Science, Utrecht University, Princetonplein 5, Utrecht 3584 CC, The Netherlands

(Received 15 September 2014; accepted 4 December 2014; published online 24 December 2014)

Many physical problems require explicit knowledge of the equilibrium shape of the interface between two fluid phases. Here, we present a new numerical method which is simply implementable and easily adaptable for a wide range of problems involving capillary deformations of fluid-fluid interfaces. We apply a simulated annealing algorithm to find the interface shape that minimizes the thermodynamic potential of the system. First, for completeness, we provide an analytical proof that minimizing this potential is equivalent to solving the Young-Laplace equation and the Young law. Then, we illustrate our numerical method showing two-dimensional results for fluid-fluid menisci between vertical or inclined walls and curved surfaces, capillary interactions between vertical walls, equilibrium shapes of sessile heavy droplets on a flat horizontal solid surface, and of droplets pending from flat or curved solid surfaces. Finally, we show illustrative three-dimensional results to point out the applicability of the method to micro- or nano-particles adsorbed at a fluid-fluid interface. © 2014 AIP Publishing LLC. [<http://dx.doi.org/10.1063/1.4904391>]

I. INTRODUCTION

Fluid-fluid interfaces are of fundamental importance for a great number of applications in soft matter. For example, the adsorption of colloids, nanoparticles, polymers, or proteins at fluid-fluid interfaces are highly relevant for industrial products (food,¹ Pickering Emulsion,^{2–4} particle synthesis,⁵ cosmetics, paints, etc.) and vital for engineering processes (washing, coating, water purification, etc.). Such phenomena have also an interest from a scientific point of view due to the specific particle-particle interactions that arise at such interfaces.^{6–12} A fundamental role in the underlying physics is played by the capillary deformations of a fluid-fluid interface when it comes into contact with a solid surface. The capillary interactions induced by these deformations can be exploited, for example, in the self-assembly of interface adsorbed colloidal particles,^{13–16} which can be directed by manipulating, e.g., the interface shape,^{17–19} the particle shape,^{20–23} or the particle concentration.^{24,25} The capillary deformations may also play an important role in the adsorption of a single non-spherical colloidal particle at a fluid-fluid interface, which is a recurrent issue in soft matter (e.g., Refs. 26–30). In recent works,^{31–36} the equilibrium configuration of such a colloidal particle has been studied theoretically, neglecting however the capillary deformations. This study is a step towards understanding the role of capillary deformations for such non-trivial geometries.

In this work, we investigate the shape of an interface between two homogeneous fluid phases in the presence of external solid surfaces and possibly gravity. We focus on the equilibrium configuration only, without taking into account the dynamics of these systems. We study the problem from a macroscopic point of view, so we treat the interface as a two-

dimensional surface with zero thickness and without capillary waves. A free energy γS is assigned to an interface with surface area S between two demixed fluids, where γ is the associated surface tension. The preferred shape of the interface is the one with minimum free energy, i.e., minimum S , which is a flat surface for a free meniscus and a spherical shape for a finite droplet without gravity. However factors like gravity, the wettability of the solids in contact with the interface, electrostatic fields, etc., influence the free energy of the interface and so deform it in a non-trivial way.

In absence of electric fields, the fluid-fluid interface shape is described by the Young-Laplace equation and Young's law (see Eqs. (18) and (24) in Sec. II). These equations, usually proved through mechanical force-balance arguments (e.g., Refs. 37–39), can be obtained using a variational principle (e.g., Refs. 40 and 41). For completeness in Sec. II, we prove this showing a short derivation (partially new, to the best of the author's knowledge) in which we minimize the total thermodynamic potential of a fluid-fluid-solid system with respect to the fluid-fluid interface shape.

As the Young and Young-Laplace equations have an analytic solution only in the simplest cases, the interface shape is usually calculated numerically. A widely used approach to calculate a minimum energy surface is by means of the Surface Evolver program.⁴² But several other approaches, both theoretical and numerical, have been used for studying the fluid-fluid interface shape in different physical problems, e.g., menisci shapes and capillary interactions,^{43–52} droplet shapes,^{53–57} diffuse interfaces,^{58–60} or fluid-fluid interfaces in contact with deformable solids.^{61–63}

In this article, we introduce a new numerical method to obtain the minimum-energy shape of a fluid-fluid interface. It

is simply implementable and easily adaptable to study a wide range of problems. Thanks to these advantages, we believe our method can be useful in future research in the soft-matter field, in particular for studying non-spherical micro- or nanoparticles at interfaces.

II. THEORY

In this section, we prove that solving the Young-Laplace equation and imposing Young's law is equivalent to minimizing the thermodynamic potential of a fluid-fluid system in contact with a solid at a fixed position. Although such a proof is widely known and accepted (a first version is due to Gauss⁶⁴), here we present a concise version for completeness. We consider (see Fig. 1) a fixed volume V that contains two demixed fluids and that is surrounded by a solid surface with fixed position. We assume the solid to be non-deformable. Henceforth, we denote the two fluids by fluid 1 and fluid 2, where fluid 1 is the lighter one. The volume and bulk mass density are, respectively, V_1 and ρ_1 for fluid 1, V_2 and ρ_2 for fluid 2, with $V_1 + V_2 = V$. The fluids are in contact with a reservoir that keeps constant the temperature T and the chemical potentials $\{\mu_i\}_{i=1}^s$, where s is the total number of chemical species present in fluid 1 and fluid 2, and μ_i is the chemical potential of the i th species. From now on, we ignore the T and $\{\mu_i\}_{i=1}^s$ dependence as they are not relevant in our derivation. We introduce a Cartesian coordinate system with the z axis anti-parallel to the gravity direction. For simplicity, we assume that the fluid-fluid interface can be written as a function $h = h(x, y)$, although our derivation can be easily extended for more general surfaces (e.g., with overhangs). The surface area of the solid wall in contact with fluid 1 is $W_1[h]$, and that with fluid 2 is $W_2[h]$, where $[h]$ means a functional dependence with respect to h . The surface tensions associated to the three interfaces fluid 1-fluid 2, solid-fluid 1, and solid-fluid 2 are γ , γ_1 , and γ_2 , respectively. We neglect in our analysis the energy contribution due to the three-phase contact line tension, although our derivation can be easily extended to include it. The total thermodynamic

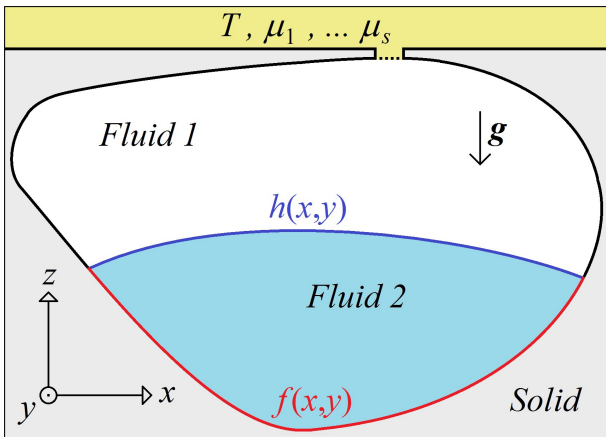


FIG. 1. Sketch of a fluid-fluid interface. The fluids are bounded by a fixed solid surface and they are in contact with a reservoir that keeps constant the temperature and the chemical potentials of all species. In blue and red are highlighted the fluid 1-fluid 2 and solid-fluid 2 interfaces, which play an important role in the derivation below.

potential of this system is

$$\Omega_t[V, h] = \gamma S[h] + \gamma_1 W_1[h] + \gamma_2 W_2[h] + E_g[h] + \Omega_1(V_1[h]) + \Omega_2(V_2[h]), \quad (1)$$

where $S[h]$ is the surface area of the fluid-fluid interface, $\Omega_1(V_1[h])$ and $\Omega_2(V_2[h])$ are the bulk grand canonical potentials of fluid 1 and 2, respectively, and $E_g[h]$ is the gravitational energy of the system, given by

$$E_g[h] = g \rho_1 \int_{V_1[h]} z d\mathbf{r} + g \rho_2 \int_{V_2[h]} z d\mathbf{r} \quad (2)$$

with $\mathbf{r} = (x, y, z)$ and g the gravity acceleration. Here, we are assuming that the two fluids have a constant mass density on a length scale at least of the order of the capillary deformations. Note that the integration domains over $V_1[h]$ and $V_2[h]$ are functionals of h .

The total area of the fluid 1-fluid 2 interface is

$$S[h] = \iint_D dx dy \sqrt{1 + h_x^2 + h_y^2}, \quad (3)$$

where D is the domain of h and $h_\alpha = \frac{\partial h(x, y)}{\partial \alpha}$, with $\alpha = x, y$. The functional derivative of S with respect to h is

$$\frac{\delta S}{\delta h(x, y)} = - \frac{h_{xx}(1 + h_y^2) + h_{yy}(1 + h_x^2) - 2h_x h_y h_{xy}}{(1 + h_x^2 + h_y^2)^{\frac{3}{2}}}, \quad (4)$$

where $h_{\alpha\beta} = \frac{\partial^2 h(x, y)}{\partial \alpha \partial \beta}$, with $\alpha, \beta = x, y$. Equation (4) can be written as

$$\frac{\delta S}{\delta h(x, y)} = \nabla \cdot \hat{\mathbf{n}}(x, y), \quad (5)$$

where $\nabla \equiv (\frac{\partial}{\partial x}, \frac{\partial}{\partial y}, \frac{\partial}{\partial z})$ and

$$\hat{\mathbf{n}}(x, y) = \frac{\nabla(z - h(x, y))}{|\nabla(z - h(x, y))|} \quad (6)$$

is the unit normal to the h surface in the point $(x, y, h(x, y))$, pointing from fluid 2 toward fluid 1. We assume now that the solid-fluid 2 interface can be written as a function $f = f(x, y)$. As before we do this for simplicity, although it is easy to extend the derivation to more general surfaces. Note that f is a functional of h , since f and h are connected at the three-phase contact line. The areas of the solid walls in contact with the fluids can be written as

$$W_2[h] = \iint_D dx dy \sqrt{1 + f_x^2 + f_y^2}, \quad (7)$$

$$W_1[h] = W - W_2[h], \quad (8)$$

where W is the total surface area of the solid in contact with the fluid-fluid system that does not depend on h . Note that the domain of f coincides here with that of h . The functional derivative of the solid-fluid surface energy with respect to h is

$$\begin{aligned} \frac{\delta(\gamma_1 W_1 + \gamma_2 W_2)}{\delta h(x, y)} &= \Delta\gamma \iint_D du dv \frac{\delta W_2}{\delta f(u, v)} \frac{\delta f(u, v)}{\delta h(x, y)} \\ &= \Delta\gamma \iint_D du dv \nabla \cdot \hat{\mathbf{N}}(u, v) \frac{\delta f(u, v)}{\delta h(x, y)} \equiv \Delta\gamma \Phi(x, y), \end{aligned} \quad (9)$$

where $\Delta\gamma = \gamma_2 - \gamma_1$, where we defined the integral as $\Phi(x, y)$ for later convenience, and where

$$\hat{\mathbf{N}}(x, y) = \frac{\nabla(z - f(x, y))}{|\nabla(z - f(x, y))|} \quad (10)$$

is the unit normal to the f surface in $(x, y, f(x, y))$, pointing from the solid toward fluid 2. The functional derivative $\delta f / \delta h$ is explicitly written as

$$\frac{\delta f(u, v)}{\delta h(x, y)} = \begin{cases} \delta(x - u)\delta(y - v), & \text{if } (x, y) \in \{\mathbf{t}\}, \\ 0, & \text{otherwise,} \end{cases}$$

where $\delta(x)$ is the Dirac delta function and $\{\mathbf{t}\}$ is the set of all the points (x, y) where $f(x, y) = h(x, y)$, i.e., such that $(x, y, h(x, y))$ is a point of the solid-fluid 1-fluid 2 three-phase contact line.

Equation (2) can be written as

$$E_g[h] = g\rho_1 \int_V z d\mathbf{r} + \frac{g\Delta\rho}{2} \iint_D (h^2 - f^2) dx dy \quad (11)$$

with $\Delta\rho = \rho_2 - \rho_1$. The functional derivative of E_g with respect to h is

$$\frac{\delta E_g}{\delta h(x, y)} = g\Delta\rho h(x, y). \quad (12)$$

Here, the $\delta f / \delta h$ term does not appear because its contribution is canceled by the h^2 term.

The grand canonical potentials can, by extensiveness, be written as

$$\Omega_1(V_1) + \Omega_2(V_2) = -P_1 V_1[h] - P_2 V_2[h], \quad (13)$$

where P_1 and P_2 are the bulk pressures of fluids 1 and 2, i.e., their pressures at the reference level $z = 0$. Using that

$$V_1[h] = V - V_2[h], \quad V_2[h] = \iint_D dx dy (h - f), \quad (14)$$

we find that

$$\frac{\delta[\Omega_1(V_1) + \Omega_2(V_2)]}{\delta h(x, y)} = -\Delta P, \quad (15)$$

with $\Delta P = P_2 - P_1$. Again, $\delta f / \delta h$ does not appear here because its contribution is canceled by the h term.

Finally, we use the minimum energy principle to state that the functional derivative with respect to h of the total thermodynamic potential Ω_t (Eq. (1)) is zero at equilibrium, that is,

$$\frac{\delta\Omega_t[h]}{\delta h(x, y)} = 0. \quad (16)$$

Using Eqs. (5), (9), (12), and (15), we obtain from Eq. (16) that

$$\gamma\nabla \cdot \hat{\mathbf{n}}(x, y) + \Delta\gamma\Phi(x, y) + g\Delta\rho h(x, y) - \Delta P = 0, \quad (17)$$

with $\Phi(x, y)$ defined in Eq. (9). First, we consider this equation for all the $(x, y) \notin \{\mathbf{t}\}$, i.e., where the interface is not in contact with the solid surface. Here, $\Phi(x, y) = 0$, so it follows:

$$\gamma\nabla \cdot \hat{\mathbf{n}}(x, y) = \Delta P - g\Delta\rho h(x, y), \quad (18)$$

which is the celebrated Young-Laplace equation. It is an equation for $h(x, y)$ at fixed ΔP , which acts as a Lagrange multiplier to set V_2 and $V_1 = V - V_2$ to the imposed volumes of fluid 2

and fluid 1, respectively. Usually in this equation, the mean curvature of $h(x, y)$ is introduced, defined as $\nabla \cdot \hat{\mathbf{n}}(x, y)/2$.

To derive the Young Law, we take Eq. (17) for any $(x, y) \in \{\mathbf{t}\}$, i.e., in a three-phase contact point, obtaining

$$\gamma\nabla \cdot \hat{\mathbf{n}}(x, y) + \Delta\gamma\nabla \cdot \hat{\mathbf{N}}(x, y) = \Delta P - g\Delta\rho h(x, y). \quad (19)$$

We now consider an infinitesimal volume dV located inside fluid 2 and in contact with the three-phase contact line. The volume dV is delimited at one face by the fluid 1-fluid 2 interface, at another face by the fluid 2-solid interface, and at the remaining three faces by planes orthogonal to the fluid 2-solid interface (see Fig. 2). We take dV small enough to assume $h(x, y)$ and $f(x, y)$ to be linear and integrate Eq. (19) over dV . The right-hand side of Eq. (19) is constant over dV in the limit $dV \rightarrow 0$ so its integration gives zero contribution in this limit. Hence, we find

$$\int_{dV} \nabla \cdot \left[\hat{\mathbf{n}}(x, y) + \frac{\Delta\gamma}{\gamma} \hat{\mathbf{N}}(x, y) \right] d\mathbf{r} = 0, \quad (20)$$

which, upon applying the divergence theorem, yields

$$\mathbf{w}(x, y) \cdot \left[\hat{\mathbf{n}}(x, y) + \frac{\Delta\gamma}{\gamma} \hat{\mathbf{N}}(x, y) \right] = 0, \quad (21)$$

where

$$\mathbf{w}(x, y) \equiv \hat{\mathbf{n}}(x, y) dS - \hat{\mathbf{N}}(x, y) dW + \hat{\mathbf{a}} dH + \hat{\mathbf{b}} dA + \hat{\mathbf{c}} dA, \quad (22)$$

with $\hat{\mathbf{n}}$, $-\hat{\mathbf{N}}$, $\hat{\mathbf{a}}$, $\hat{\mathbf{b}}$, and $\hat{\mathbf{c}}$ the normals toward outside of the various faces of dV (see Fig. 2). The areas of these faces are, respectively, dS , dW , dH , dA , and dA . By definition of dV , we have $\hat{\mathbf{n}} \cdot \hat{\mathbf{b}} = \hat{\mathbf{n}} \cdot \hat{\mathbf{c}} = \hat{\mathbf{N}} \cdot \hat{\mathbf{a}} = \hat{\mathbf{N}} \cdot \hat{\mathbf{b}} = \hat{\mathbf{N}} \cdot \hat{\mathbf{c}} = 0$. We call θ the angle formed by the fluid 1-fluid 2 interface with the solid-fluids interface and measured inside fluid 2 (so inside dV). Therefore, $\hat{\mathbf{n}} \cdot \hat{\mathbf{a}} = -\sin\theta$ and $\hat{\mathbf{n}} \cdot \hat{\mathbf{N}} = \cos\theta$. Then by definition of the normal $\hat{\mathbf{n}} \cdot \hat{\mathbf{n}} = \hat{\mathbf{N}} \cdot \hat{\mathbf{N}} = 1$, and hence from Eq. (21), it follows that:

$$\frac{\Delta\gamma}{\gamma} = \frac{\cos\theta dW + \sin\theta dH - dS}{\cos\theta dS - dW}. \quad (23)$$

If we use now that $dH = \sin\theta dS$, we obtain

$$\frac{\gamma_1 - \gamma_2}{\gamma} = \cos\theta, \quad (24)$$

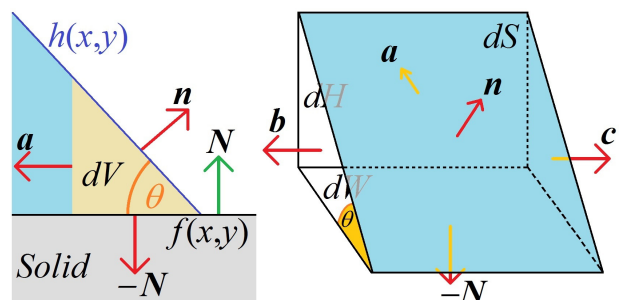


FIG. 2. Profile and 3D view of the infinitesimal volume dV on which we integrate Eq. (19). We chose dV small enough to consider $h(x, y)$ and $f(x, y)$ linear within it. One face of dV is the fluid 1-fluid 2 interface (colored in blue in the picture on the right), and it has normal $\hat{\mathbf{n}}$ and area dS . Another face of dV is the solid-fluid 2 interface, with normal $-\hat{\mathbf{N}}$ and area dW . The remaining three faces of dV are orthogonal to the solid-fluid 2 interface and have, respectively, normal $\hat{\mathbf{a}}$, $\hat{\mathbf{b}}$, and $\hat{\mathbf{c}}$ and area dH , dA , and dA .

which is Young's law. It tells that the contact angle of the fluid 1-fluid 2 interface with the solid surface is univocally fixed by the three surface tensions.

We have thus proven that minimizing the potential Ω_t of a fluid-fluid-solid system (Eq. (1)) with respect to the fluid-fluid interface shape is equivalent to solving the Young-Laplace equation and the Young law.

III. NUMERICAL METHOD

In our method, we find the equilibrium shape of a fluid-fluid interface for a given volume of each fluid. This is done by calculating numerically the interface shape that minimizes the following thermodynamic-potential functional:

$$E = \gamma S + (\gamma_2 - \gamma_1) V_2 + g \Delta \rho \int_{V_2} z d\mathbf{r}, \quad (25)$$

with the constraint that the volumes V_1 and V_2 of fluid 1 and fluid 2 have a preset value. Here, S is the area of the fluid 1-fluid 2 interface, V_2 is the area of the solid surface in contact with fluid 2. We recall that S , V_2 , V_1 , V_2 , and E are functional of the fluid-fluid interface shape. From the Lagrange multipliers theorem, it follows that we are minimizing the potential:

$$\Omega_t = E - P_1 V_1 - P_2 V_2, \quad (26)$$

where the Lagrange multipliers P_1 and P_2 depend on the choice of V_1 and V_2 . This expression for Ω_t is identical to Eq. (1), except for a shift in the energy reference level not depending on the fluid-fluid interface shape. Therefore, the interface shape that we calculate minimizing Ω_t (Eq. (26)) is the one that solves the Young-Laplace equation and the Young Law, as proved in Sec. II. For convenience, we rewrite E (Eq. (25)) as

$$E = \gamma \left[S - W_2 \cos \theta + \ell^{-2} \int_{V_2} z d\mathbf{r} \right], \quad (27)$$

where

$$\ell = \sqrt{\frac{\gamma}{g \Delta \rho}} \quad (28)$$

is the capillary length and $\cos \theta$ is defined by Eq. (24). Thus, given the fluid volumes and the configuration of the external solid surfaces, the input parameters that determine the shape of the fluid-fluid interface are $\cos \theta$ and ℓ .

For simplicity and illustration purpose, we consider here systems with translational invariance along the Cartesian coordinate y , so that the fluid-fluid interface can be represented by a 2D profile (but a generalization of our method to 3D systems without symmetries is straightforward and will be presented elsewhere). We represent the interface profile using a set of points forming a 1D grid, as shown in Fig. 3. We indicate the two extreme points of the grid with C_1 and C_2 , which are constrained to stay on the imposed solid boundaries of the fluid-fluid system. We call the remaining points \mathbf{P}_i ($i = 1, \dots, N$) "free points," and these are allowed to be wherever outside the solids in the (x, z) -plane. The interface is given by the set of segments linking any two consecutive points (by definition, \mathbf{P}_{i+1} is consecutive to \mathbf{P}_i , \mathbf{P}_1 to C_1 and C_2 to \mathbf{P}_N). The fluid volume is set by the initial positions of the grid points. The interface equilibrium shape follows from the positions of

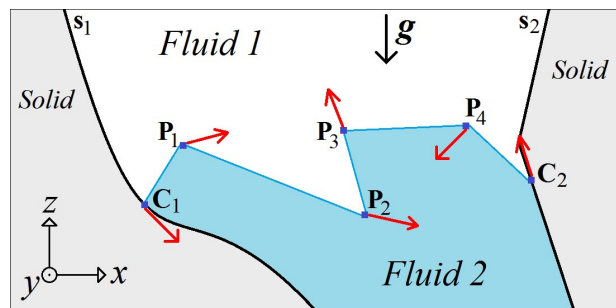


FIG. 3. In our numerical method, the fluid-fluid interface is represented by a set of points P_1, P_2, \dots attached to k solid walls at C_k ($k = 1, 2$ here). In the simulation, these points are continuously moved until the configuration that minimizes E (Eq. (27)) for fixed volumes V_1 and V_2 of the fluids is found.

the points that minimize E (Eq. (27)) fulfilling the constraint of a fixed volume for the fluids. To find these positions, we apply a simulated annealing algorithm,⁶⁵ that is an adaptation of a Monte Carlo method, where a temperature is artificially introduced and gradually lowered during the simulation. This drives the system toward its minimum energy configuration in a way that resembles an annealing process, from which the name of the method is derived. In our model, we change randomly the point positions, keeping the fluid volumes V_1 and V_2 constant and not allowing unphysical configurations (e.g., self-intersecting, see Appendix). Every configuration change is then accepted with probability

$$\mathcal{P} \equiv \begin{cases} 1, & \text{if } \Delta E < 0 \\ \exp\left(-\frac{\Delta E}{k_B T}\right), & \text{if } \Delta E \geq 0 \end{cases}, \quad (29)$$

where ΔE is the variation of E (Eq. (27)) between the old and the new configuration of the points, and T is the temperature-like control parameter (k_B is the Boltzmann constant). In the simulation, these configuration changes are performed continuously while T is gradually lowered starting from an initial T_0 . When T becomes zero, the simulation ends. Thanks to the randomness involved, the simulated annealing has the advantage of providing escape routes out of metastable states, unlike energy-gradient methods. However, the speed of the T decrement and the initial value T_0 must be chosen slow and high enough, respectively. To avoid metastable states, $k_B T_0$ needs to be much bigger than the energy barrier of these states. An adequate choice of T_0 and its decrement speed depends on the discrepancy between the initial configuration of the points and the final solution. As a general rule: The slower is the decrement of T , the better is the approximation of the final solution. If different equivalent global minima of the energy are present, then the method finds randomly only one of these. A detailed description on the implementation of our method is provided in the Appendix.

It is worth to mention that our method can be adapted to work at constant pressure instead of constant volume by removing the constraint of a fixed volume and by minimizing the potential Ω (Eq. (26)), instead of E (Eq. (27)). This can be useful, for example, for studying curved fluid-fluid interfaces.

IV. RESULTS

We present some results as obtained from our method. The main aim of this section is to show that this method is applicable to a wide range of physical problems involving the equilibrium shape of fluid-fluid interfaces. All the systems shown here have translational invariance along the y direction, pointing out of the paper. The simulation parameters (N , T_0 , etc.) used for the various results are reported in Table II of the Appendix.

A. Meniscus close to a vertical wall

First, to prove the accuracy of the method, we consider the case of a fluid-fluid interface in the half-space $x > 0$ close to a vertical wall located in the plane $x = 0$. In this case, it is known analytically that the height profile $z(x)$ of the meniscus is expressed^{66,67} by the inverse relation

$$\frac{x(z)}{\ell} = \operatorname{acosh}\left(\frac{2\ell}{|z|}\right) - \operatorname{acosh}\left(\frac{2\ell}{|z_0|}\right) - \sqrt{4 - \frac{z^2}{\ell^2}} + \sqrt{4 - \frac{z_0^2}{\ell^2}}, \quad (30)$$

where z is negative if $\cos \theta \leq 0$ and positive otherwise, and the contact height $z_0 = z(0)$ is given by

$$z_0^2 = 2\ell^2(1 - \sin \theta). \quad (31)$$

In Fig. 4, we show the interface profiles obtained from our numerical method with $N = 28$ free points of the grid for different values of $\cos \theta$. For comparison, we also plot the corresponding analytical solutions of Eq. (30), which are indistinguishable from our numerical curves. To reproduce the flatness of the meniscus for $x \rightarrow \infty$, we placed another vertical wall with contact angle $\pi/2$ at $x = 20\ell$ (i.e., far beyond the scale of Fig. 4). All the numerical and analytical solutions

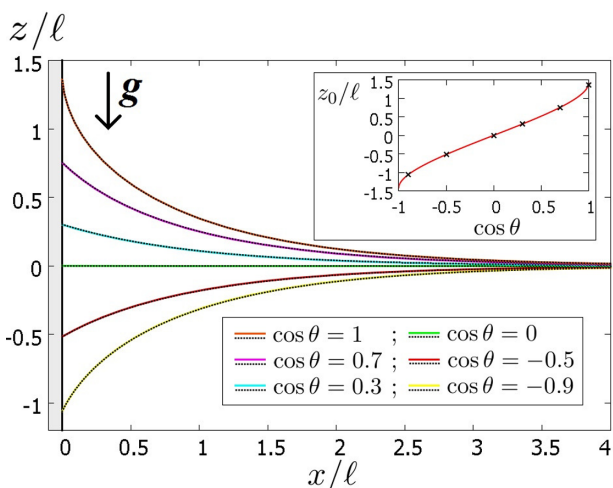


FIG. 4. Height profiles $z(x)$ of fluid-fluid menisci with capillary length ℓ close to a vertical wall in the plane $x = 0$ for different contact angles θ . The full lines are obtained numerically from our algorithm and shifted in z to have the same asymptotic height for $x \rightarrow \infty$. The dotted lines are the analytical solutions from Eq. (30), indistinguishable from the numerical curves. In the inset, the numerical values of the capillary rise z_0 (black crosses) are compared with the analytic result of Eq. (31) (full line).

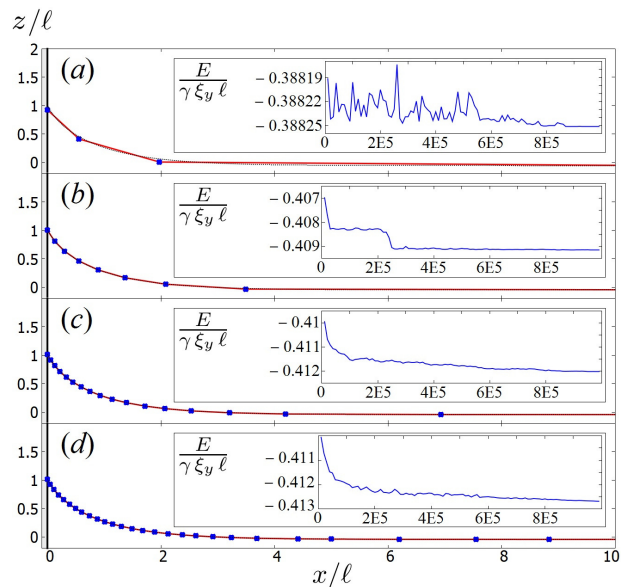


FIG. 5. Height profile $z(x)$ of a fluid-fluid meniscus close to a vertical wall in $x = 0$ with contact angle θ and $\cos \theta = 0.9$. We show the numerical solutions obtained using a grid with a different number of free points ((a): $N = 3$; (b): $N = 8$; (c): $N = 18$; (d): $N = 38$) and the points are plotted in the graph. On the right in the half-space $x > 20\ell$, the fluid-fluid system is limited by a vertical wall with contact angle $\pi/2$. For convenience, we show the solution only in the region $x \in [0, 10\ell]$. The dotted lines are the analytical solutions from Eq. (30) shifted in z to match our solutions at $x = 20\ell$. The initial configuration of the points is an equally spaced grid on the x -axis. The final profiles indicate migration of the points during the simulation to pack more on the curved part of the interface. The insets show the behavior of the energy E (Eq. (27), ξ_y is the length of the system in y) with respect to the number of cycles performed in the simulation. These graphs prove that during the simulation, the system evolves toward configurations with lower energy, the more so for a larger number of grid points N .

shown are slightly shifted in z such that $z(20\ell) = 0$. The inset of Fig. 4 also shows excellent agreement between our numerical results and the analytic expression Eq. (31) of the contact height.

In Fig. 5, we study the influence of the number of points on the solution. We consider the system of Fig. 4 for the case $\cos \theta = 0.9$, and we show the numerical solutions we obtain using a grid with (a) $N = 3$, (b) $N = 8$, (c) $N = 18$, and (d) $N = 38$ free points, respectively. For convenience, the solution is shown for $x \in [0, 10\ell]$, while the right limit of the system is in $x = 20\ell$, so not all the points of the solution are visible in the figure. We see that even for a few points, our numerical solution matches fairly well with the analytical one (dotted line). It is interesting to note that the density of points is higher where the interface is curved and lower in the flat region. The initial configuration, however, was an equally spaced grid on the x -axis. Therefore during the simulation, the points have spontaneously migrated to increase their density on the curved part of the interface. This disposition allows the points to optimize the energy and so to find the deepest minimum. In the insets of each graph of Fig. 5, we plot the energy E (Eq. (27)) of the system with respect to the number of cycles performed in the simulated annealing process. One cycle corresponds to the execution until the last step of the algorithm reported in the Appendix. The energy converges towards a minimum value in

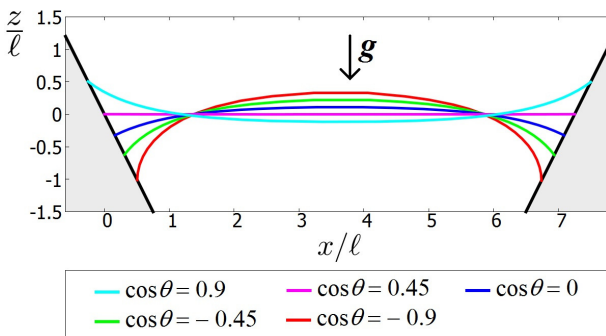


FIG. 6. Height profiles $z(x)$ of fluid-fluid menisci between two inclined walls. Each line is a solution obtained numerically from our algorithm using a certain value of $\cos \theta$ in the potential E (Eq. (27)). The volumes of the fluids are the same for every solution.

all the simulations, with a lower energy at higher number of grid points N , i.e., the approximation of the numerical solution improves by increasing N . Therefore, a good way to choose a proper value for N is to repeat the simulation using higher values of N , until the energy of the final solution does not vary anymore (within the desired precision).

The relatively small number of points needed to describe the interface is important to generalize to two-dimensional interfaces (i.e., three-dimensional systems).

B. Meniscus between flat and/or curved surfaces

Our numerical method is very general and allows to consider solid boundaries of any shape, which is important for future studies of odd-shaped nano-particles for instance. In this subsection, we provide some examples presenting results for fluid-fluid menisci located between inclined walls and/or curved surfaces.

In Fig. 6, we show some numerical solutions for the shape of a meniscus between two inclined walls. The two walls are symmetric with respect to a central vertical axis and as expected also the solutions fulfill this symmetry. Another indication of the correctness of our method is given by the contact angle that each numerical solution forms with the two solid surfaces. The numerical value θ^* of the contact angle of the meniscus with each solid surface is calculated from the positions of the point of the interface grid constrained on that surface and its first neighbor (\mathbf{P}_1 for C_1 and \mathbf{P}_N for C_2). The obtained values of $\cos \theta^*$ for each solution match very well with the input parameter $\cos \theta$; in particular, we find that $|\cos \theta^* - \cos \theta| < 0.05$ in all cases. A higher precision can be achieved by increasing the number of points N of the interface.

In Fig. 7, we present analogous results for fluid-fluid menisci located between a curved surface and an inclined wall (a), and inside a cylindrical cavity with symmetry axis pointing out of the paper (b). In both these systems, the numerical solutions are obtained using different values of $\cos \theta$ and different volumes for fluid 2 (the fluid below). We see that, as expected, the meniscus adapts its shape upon changing the fluid volume to keep its contact angles with the external surfaces constant. We point out once more that we are not imposing *a priori* this

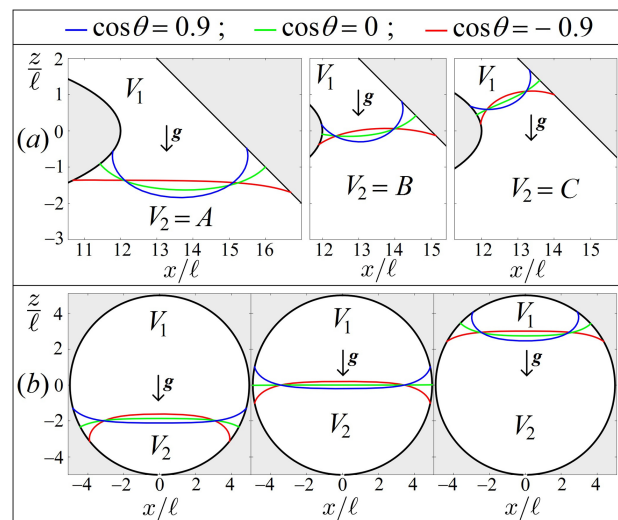


FIG. 7. Height profiles $z(x)$ of fluid-fluid menisci either between a curved surface and an inclined wall (a) or inside a cylindrical cavity with symmetry axis pointing out of the paper (b). Each line is a solution obtained numerically from our algorithm using a certain value of $\cos \theta$, indicated in the graph. In each graph, the solutions are obtained assigning a different volume V_2 to the heavier fluid 2((a)): $A < B < C$; (b) from left to right: $V_2/V = 0.23$, $V_2/V = 0.5$, and $V_2/V = 0.83$.

constraint for the contact angles of the meniscus, but this is automatically obtained upon minimizing the thermodynamic potential E (Eq. (27)) of the system.

C. Capillary interaction

In this section, we present results on the capillary interaction between two vertical flat walls, although solid surfaces with any other shape can be taken into account as well.

In Fig. 8, we consider a system of two vertical walls, each of width 1ℓ , immersed in the fluid-fluid interface and at a surface-to-surface distance D from each other. The origin of the x axis is in the middle between the two walls. The whole fluid-fluid system is enclosed between two external vertical walls in the half-planes $x < -15\ell$ and $x > 15\ell$, respectively, far beyond the scale of the graphs in Fig. 8. Three one-dimensional grids of points are necessary to represent the interface: One set between the two inner central walls and the other two between the external walls and the central walls. During the simulation, fluid 2 can exchange volume between these three regions, but the sum of the volumes below the three interfaces is kept constant. The central wall on the left has contact angle θ_l , the one on the right θ_r . We assign a contact angle $\theta = \pi/2$ to the two external walls, to induce a flat meniscus far from the two central walls in order to mimic an infinite system. To consider in our model the presence of solid surfaces with different contact angles, we generalize Eq. (27) to

$$E = \gamma \left[S - \sum_k W_2(k) \cos \theta_k + \ell^{-2} \int_{V_2} z d\mathbf{r} \right], \quad (32)$$

where the k -sum is over all the solid walls, θ_k is the contact angle of the k th solid surface, and $W_2(k)$ is its surface area in contact with fluid 2. In the system of Fig. 8, we have $k = 2$, with the two solid walls referred to as left (l) and right (r).

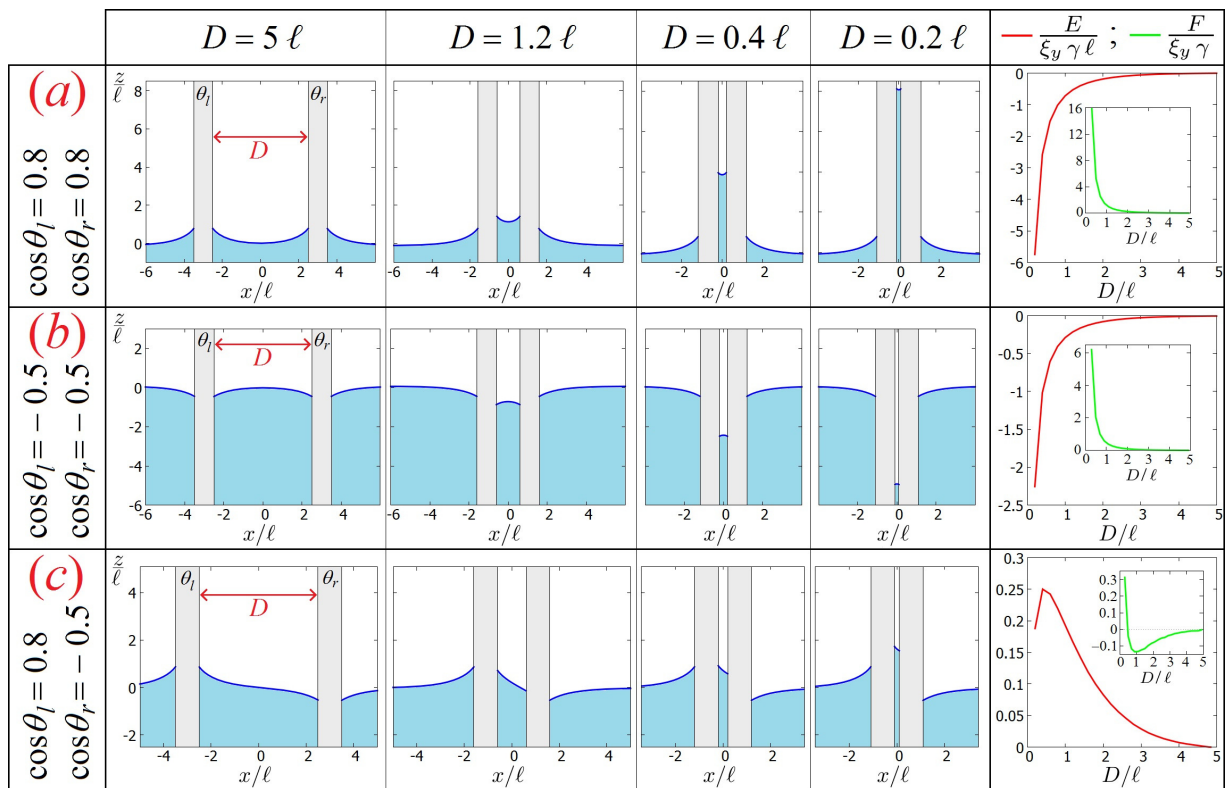


FIG. 8. Left: Height profile of a horizontal fluid-fluid interface in contact with two vertical walls of width 1ℓ . The system has translational invariance in the y direction and it is limited by two external walls with contact angles $\pi/2$ in the half-spaces $x > 15\ell$ and $x < -15\ell$, beyond the scale of the plot. The central wall on the left has contact angle θ_l , the one on the right θ_r . The interface shape is calculated numerically by our method and it is shown for different surface-to-surface distances D between the walls for (a) $\cos\theta_l = \cos\theta_r = 0.8$; (b) $\cos\theta_l = \cos\theta_r = -0.5$; (c) $\cos\theta_l = 0.8, \cos\theta_r = -0.5$. Right: The effective interaction potential $E(D)$ (Eq. (32)) of the system. The capillary force $F(D) \equiv dE/dD$ acting between the walls is plotted in the insets.

For the system considered in Fig. 8, we have calculated the shape of the fluid-fluid interface for several surface-to-surface distances between the left and right wall, using as contact angles: (a): $\cos\theta_l = \cos\theta_r = 0.8$; (b): $\cos\theta_l = \cos\theta_r = -0.5$; (c) $\cos\theta_l = 0.8$ and $\cos\theta_r = -0.5$. In Fig. 8(a), we see the capillary rise of the interface obtained by decreasing D , and in Fig. 8(b), we see the capillary drop. The height of the capillary rise is greater than the depth of the capillary drop—at the same D —because in the former case the contact angle has a larger absolute value. In case (c), we see the interface shape due to the interplay between a capillary rise and drop.

For each of the cases (a), (b), and (c) of Fig. 8, we report on the very right the effective potential $E(D)$ and the force $F(D)$ of the capillary interaction between the two central walls, defined as $F \equiv dE/dD$. Here, $E(D)$ is the minimum of the functional of Eq. (32) and it is computed as described in the appendix. In the insets, we show $E(D)$ shifted to be zero at $D = 5\ell$. We consider F only for $D \leq 5\ell$, such that the minimum distance between the central walls and the external walls always exceeds 10ℓ . So we can reasonably assume that the effects of the external walls on F are negligible. For both the cases (a) and (b), we see an attractive force. In (a), the force is stronger than in (b) because the absolute value of the contact angle is greater. In (c), we observe a repulsive force at large separations due to the fact that $\cos\theta_l$ and $\cos\theta_r$ have different signs. However, there is a maximum in $E(D)$ for $D \approx 0.5\ell$ and so an attractive force between the walls exists when they are closer than about 0.5ℓ . This is caused by the different absolute values of $\cos\theta_l$ and

$\cos\theta_r$ which generate a slight capillary rise for small D , as we can see in Fig. 8(c).

In Fig. 9, we report the D dependence of the capillary rise z_c between the two walls at $x = 0$ for the cases (a) and (b) of Fig. 8. The reference level $z = 0$ is the height of the interface at $x = \pm 15\ell$. Our numerical values (symbols) are compared with an approximate analytical result (line) given by

$$z_c = \frac{2\ell^2}{D} \cos\theta. \quad (33)$$

Equation (33) follows from the approximation, valid for two narrow vertical walls, that the meniscus between them has a cylindrical shape. To check this, use that the mean curvature $\nabla \cdot \hat{\mathbf{n}}/2$ of a surface can be written as $-(\kappa_1^{-1} + \kappa_2^{-1})$, where κ_1 and κ_2 are the two radii of curvature. For the central point of a meniscus with cylindrical shape, we have $\kappa_1 = R$, with R the radius of the circular section of the cylinder, and $\kappa_2 = \infty$. Then applying Eq. (18) for $x \rightarrow \pm 15\ell$, we have that $\Delta P = 0$, because here $\nabla \cdot \hat{\mathbf{n}} = 0$, as the interface is flat, and $h = 0$ for the choice of the reference level. So the Young-Laplace Eq. (18) for the central point of the meniscus becomes $2\gamma/R = g\Delta\rho z_c$. Equation (33) follows using that $D = 2R\cos\theta$ (see Fig. 8(c), right panel). The agreement of our numerical values with Eq. (33) is quite good for $D < \ell$, confirming that the approximation of a cylindrical shape for the meniscus is good for small D .

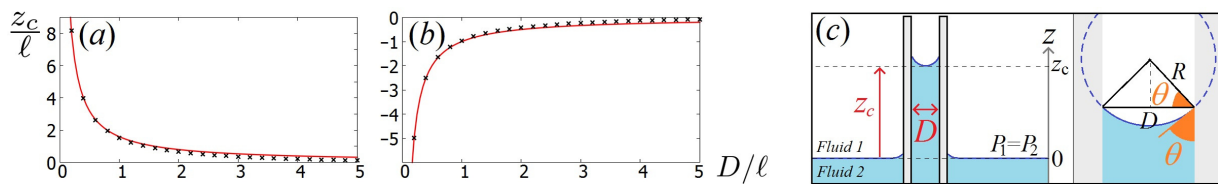


FIG. 9. Capillary rise z_c of the central point of a meniscus between two vertical walls for (a) $\cos \theta = 0.8$ and (b) $\cos \theta = -0.5$, with respect to the surface-to-surface distance D between the walls (the meniscus equilibrium shape is shown for some values of D in Fig. 8). The symbols are our numerical values, the line is the analytical result from Eq. (33), obtained by approximating the meniscus with a cylindrical shape. Our results confirm that the larger is D , the poorer is this approximation. In (c), right panel, a meniscus with a cylindrical shape is sketched.

D. Two-dimensional sessile and pendant droplets

In this subsection, we show that our numerical method is also usable for studying equilibrium shapes of droplets. Recall that here, we only consider two-dimensional droplets.

In Fig. 10, we report the equilibrium shape of a two-dimensional sessile droplet on a flat solid surface. The droplet is formed by fluid 2, which is the heavier of the two fluids. The numerical solutions are computed using different values of ℓ and $\cos \theta$. Considering γ and the volume of the droplet as fixed constants, it follows that a lower ℓ corresponds to a higher $\Delta\rho$, i.e., to a heavier droplet. As a matter of fact in each graph of Fig. 10, we see that, for droplets with the same volume and contact angle, the effect of the gravity on the droplet shape increases by lowering ℓ . As shown, our method is able to treat also the extreme case of low wettability (we see the case $\cos \theta = -0.9$ in the third graph of Fig. 10). As another indication of the correctness of the method, the equilibrium shapes are symmetric with respect to a central symmetry axis (in the figure, the solutions are shifted in x to align their axes). Moreover, as expected, our solutions show that by decreasing ℓ , the effect of the gravity on the droplet shape is increased. As said before, under a certain value of ℓ , our method does not find an equilibrium configuration for the pendant droplet, that is, the grid points keep going in the direction of \mathbf{g} until the simulation ends. For a fixed volume of the droplet, we found that this limit value ℓ^* increases by lowering $\cos \theta$.

The value of ℓ^* we obtained for the three contact angles considered in Fig. 11(a) is reported in Table I. However, we point out that there could be a certain inaccuracy in this value. Indeed, a simulation with ℓ below ℓ^* can still produce a stable equilibrium shape for the pendant droplet if the annealing is too fast or the initial temperature T_0 is too low. This happens because the grid points, that during the simulation would keep going in the direction of \mathbf{g} (as $\ell < \ell^*$), get trapped in a metastable state, and so they form a metastable equilibrium shape instead of falling down. The closer is ℓ to ℓ^* (with $\ell < \ell^*$), the slower the annealing and the higher T_0 need

given by Eq. (34), and in this case, the minus sign multiplying ℓ^2 is needed because $\Delta\rho$ is negative (see Eq. (25)). Therefore, the results we present for pendant droplets are likewise valid for sessile droplets lighter than the fluid outside.

If the gravitational force is too strong, i.e., ℓ too low, then our method does not find an equilibrium configuration (all the free points of the interface keep going in the direction of \mathbf{g} until the simulation stops). This corresponds to the physical situation in which the pendant droplet detaches itself or partially falls down.

In Fig. 11(a), we see equilibrium shapes of pendant droplets from a flat solid surface, obtained numerically using different values of ℓ and $\cos \theta$. As an indication of the correctness of our method, the equilibrium shapes are symmetric with respect to a central symmetry axis (in the figure, the solutions are shifted in x to align their axes). Moreover, as expected, our solutions show that by decreasing ℓ , the effect of the gravity on the droplet shape is increased. As said before, under a certain value of ℓ , our method does not find an equilibrium configuration for the pendant droplet, that is, the grid points keep going in the direction of \mathbf{g} until the simulation ends. For a fixed volume of the droplet, we found that this limit value ℓ^* increases by lowering $\cos \theta$. The value of ℓ^* we obtained for the three contact angles considered in Fig. 11(a) is reported in Table I. However, we point out that there could be a certain inaccuracy in this value. Indeed, a simulation with ℓ below ℓ^* can still produce a stable equilibrium shape for the pendant droplet if the annealing is too fast or the initial temperature T_0 is too low. This happens because the grid points, that during the simulation would keep going in the direction of \mathbf{g} (as $\ell < \ell^*$), get trapped in a metastable state, and so they form a metastable equilibrium shape instead of falling down. The closer is ℓ to ℓ^* (with $\ell < \ell^*$), the slower the annealing and the higher T_0 need

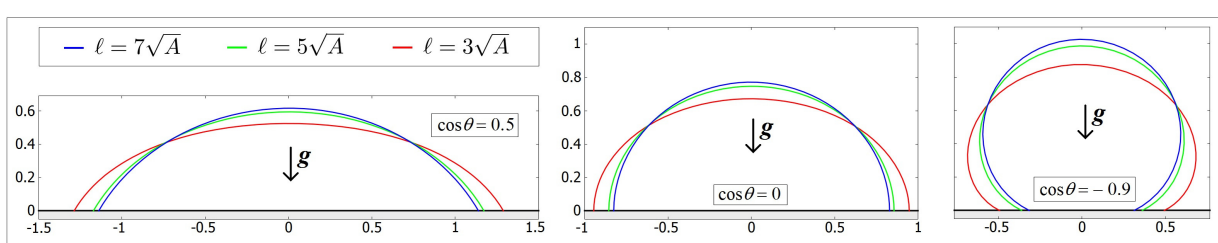


FIG. 10. Equilibrium profiles of a 2D sessile droplet on a flat solid surface. The fluid forming the droplet is heavier than the fluid outside. The solutions are obtained numerically from our method using different values of $\cos \theta$ and ℓ in the potential E (Eq. (27)). The vertical axis is z/\sqrt{A} and the horizontal axis x/\sqrt{A} , with A the area of the two-dimensional droplet. As expected, our solutions show for a fixed $\cos \theta$ an increasing flattening of the droplet shape with decreasing ℓ .

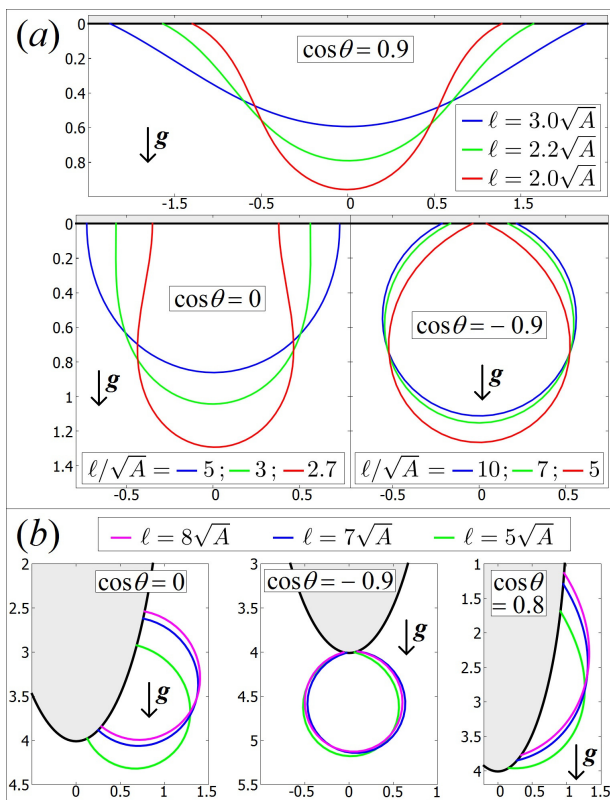


FIG. 11. Equilibrium profiles of a 2D droplet pending from (a) a flat solid surface; (b) a highly curved solid surface. The fluid forming the droplet is heavier than the fluid outside. The solutions are obtained numerically by our method using different values of $\cos \theta$ and ℓ in the potential E (Eq. (34)). The vertical axis is z/\sqrt{A} and the horizontal axis x/\sqrt{A} , with A the area of the droplet. As expected our solutions show that, for a fixed $\cos \theta$, decreasing the value of ℓ means to increase the gravity effect on the droplet shape. Moreover, the results in (b) show that, by changing the wettability of the system, the droplet prefers to wet a solid surface with a different curvature. Therefore, its minimum energy position on the solid surface changes with respect to $\cos \theta$.

to be in order to see the droplet collapsing and so to recognize that $\ell < \ell^*$.

In Fig. 11(b), we show analogous results but for the equilibrium shape of droplets pending from a highly curved solid surface. The solid surface is symmetric with respect to a central symmetry axis, and indeed—for fixed $\cos \theta$, ℓ , and droplet volume—two different solutions exist, one being the mirror image of the other with respect to this axis (in a single simulation, our method finds randomly one of these two solutions, and in the graphs, we show only the solutions on one side of the solid surface). It is interesting to observe that the minimum-energy equilibrium shape of the pendant droplet changes its position on the curved surface if we tune the wettability of the system. This is reasonable due to the fact that a droplet

TABLE I. The limit value ℓ^* of ℓ , below which the two-dimensional pendant droplet shapes calculated by our numerical method are not stable. With A , we refer to the area of the droplet. As shown, ℓ^* depends on the contact angle θ of the droplet. For ℓ above ℓ^* , some equilibrium pendant droplet shapes are plotted in Fig. 11(a).

$\cos \theta$	-0.9	0.0	0.9
ℓ^*/\sqrt{A}	3.1	2.7	2.0

with a different contact angle prefers a different curvature of the solid surface that it is wetting; for high contact angles, the droplet prefers a lowly curved convex surface rather than a highly curved one, and for low contact angle, it prefers a highly curved convex surface. Therefore, the final position of the droplet on the heterogeneously curved solid surface is given by an interplay between gravitational force, fluid-fluid, and fluid-solid interactions.

V. SUMMARY AND CONCLUSIONS

We have introduced a new numerical method able to calculate the equilibrium shape of a fluid-fluid interface in the presence of external solid surfaces and possibly gravity. First in Sec. II, we have presented a short proof that the Young-Laplace Eq. (18) and Young's Law (24) derive from the minimization of the thermodynamic potential (Eq. (1)) of the fluid-fluid system. Then in Sec. III, we have illustrated our method, providing in the Appendix a detailed description of the algorithm implementation for 1D fluid-fluid interfaces. Finally in Sec. IV, we have presented some results to show the applicability of this method to a wide range of problems.

In Sec. IV A, we have proved the correctness of our numerical method showing an excellent agreement between numerical and analytical solutions. In Sec. IV B, we have reported the shape of menisci in contact with vertical or inclined walls and curved surfaces to show the possibility of considering any kind of shape for the solid surfaces in contact with the interface. This is relevant for future applications to colloidal particles of various shapes. In Sec. IV C, we have exploited our method to study the capillary rise and capillary interactions. In this paper, we have considered the capillary interaction between vertical flat solid surfaces, although the same analysis can be done for solid surfaces with any shape. We have shown how the magnitude and the sign of the capillary interaction between the two solids change by tuning the solids contact angle and distance. In Sec. IV D, we have applied our numerical method to study the equilibrium shape of two-dimensional droplets. In principle, three-dimensional droplets can be studied with the same method, and results about this will be presented elsewhere. We have considered both sessile droplets on a horizontal flat solid surface and pending droplets from flat horizontal and curved solid surfaces. We have shown how their shape varies by tuning the wettability and the weight of the droplet. We have also pointed out that by our method, we can study the preferred position of the droplet on the solid with respect to the solid surface curvature.

To focus on the basic ingredients of the method and on the fundamental underlying physics, in this work, we have considered only systems with translational invariance along a direction orthogonal to the gravity vector, i.e., represented by a 1D fluid-fluid interface. However, the method can be applied to generic 3D systems, i.e., requiring 2D fluid-fluid interfaces. In particular, we believe that our numerical method is very valuable for the study of adsorbed micro- or nanoparticles at fluid-fluid interfaces. To show that the method can indeed be applied to this kind of 3D problems, we report in Fig. 12(a), the equilibrium shape of a fluid-fluid interface

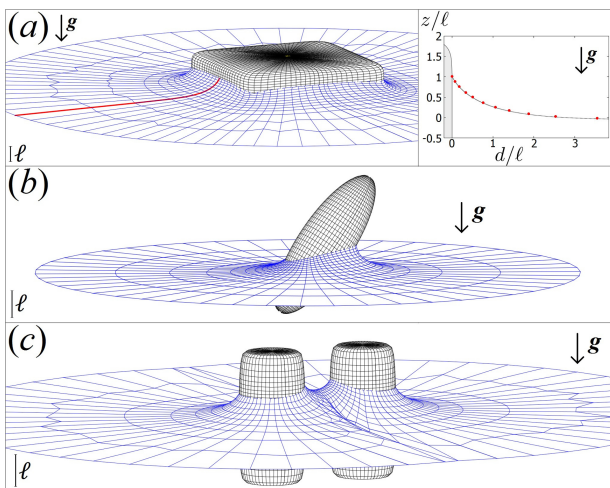


FIG. 12. 3D views of the equilibrium shape of a fluid-fluid interface (blue grid) close to solid particles (black grid) with a fixed position and with contact angle θ such that $\cos \theta = 0.9$. The gravity direction is anti-parallel to z . If no solid particle is present, the fluid-fluid interface coincides with the $z = 0$ plane. The system is surrounded by a solid vertical wall with contact angle $\pi/2$. The equilibrium shape of the fluid-fluid interface is obtained through our numerical method by minimizing E (Eq. (27)) for a fixed volume of the fluids. The scale bar is equal to the capillary length ℓ . In (a), left panel, there is a $10\ell \times 10\ell \times 4\ell$ solid parallelepiped with center of mass at $z = 0$ and with its four $10\ell \times 4\ell$ faces parallel to the z direction. In (a), right panel, the height profile of the fluid-fluid interface is shown along the red line marked in the 3D view in the left panel, with d the distance from the particle surface. The red dots are the positions of the fluid-fluid interface grid points obtained numerically by our method. The dotted line is the analytic solution of Eq. (30). In (b), there is a solid ellipsoid with the long axis equal to 6ℓ and the short axes equal to 2ℓ , inclined with angle $\pi/5$ with respect to its vertical position, and with center of mass at $z = \ell$. In (c), there are two solid vertical cylinders with height 2ℓ , radius ℓ , center of mass in $z = 0$, and with a surface-to-surface distance equal to ℓ .

close to a solid parallelepiped with a fixed position, horizontal with respect to the unperturbed fluid-fluid interface plane. The horizontal sides of this particle are ten times the capillary length ℓ . Therefore, each vertical face of the particle is large enough with respect to ℓ to behave as a vertical wall for the fluid-fluid interface if we stay far enough from the particle corners. Indeed, see the right panel in Fig. 12(a), the fluid-fluid interface height profile, as obtained numerically by our method, matches with the analytical prediction of Eq. (30) along a direction perpendicular to a vertical face of the particle, confirming the correctness of the method. Our method can be applied to calculate the fluid-fluid interface equilibrium shape close to particles with any shape, position, and orientation (e.g., see a tilted ellipsoid in Fig. 12(b)). This allows to study the adsorption potential of isolated particles with respect to their configuration with the effects of the capillary deformations included. Another appealing application of our method is the study of the capillary interactions between two or more adsorbed particles (e.g., see in Fig. 12(c) the capillary bridge between two vertical solid cylinders). Besides, thanks to its simplicity and flexibility, this method can handle a wide range of situations, e.g., involving janus-like particles and rough particles with a pinned triple contact line.

To obtain the results of Fig. 12, we exploited the numerical method introduced in this paper, but with a 2D grid of points to represent the fluid-fluid interface. The simulation time required

was of the order of minutes, using an ordinary office PC. In the Appendix of this paper, we provide a detailed description of the method implementation for 1D fluid-fluid interfaces. An analogous description of the method implementation for 2D fluid-fluid interfaces will be provided elsewhere. Specific results on the adsorption and behavior of colloidal particles at fluid-fluid interfaces will also be presented in the near future.

Aside from adsorbed colloidal particles, our numerical method can be applied and adapted to study a wide range of other physical problems relevant in soft matter and involving (equilibrium shapes of) fluid-fluid interfaces, e.g.: droplets on super-hydrophobic or structured solid substrates,^{68,69} fluid-fluid interfaces in contact with deformable solid surfaces,^{61–63} and fluid droplets adsorbed at a fluid-fluid interface.^{70,71}

ACKNOWLEDGMENTS

The authors acknowledge financial support by a “Nederlandse Organisatie voor Wetenschappelijk Onderzoek” (NWO) Vici Grant and by the Marie Curie Initial Training Network “Soft Matter at Aqueous Interfaces” (SOMATAI). This work is part of the D-ITP consortium, a program of the NWO that is funded by the Dutch Ministry of Education, Culture, and Science (OCW).

APPENDIX: ALGORITHM IMPLEMENTATION

Here, we report in detail how we have implemented our numerical method. The physical system of interest has translational invariance along y for convenience (with the gravity anti-parallel to z). Therefore, we consider a (x,z) -plane and we minimize the potential $\varepsilon \equiv E/(\gamma \xi_y)$ with respect to the fluid-fluid interface shape, where E is defined by Eqs. (27) and (32), and ξ_y is the length of the system along y . The algorithm is as follows:

- Assuming we have two solid surfaces that enclose our system, we introduce the two parametric functions $s_1(u)$ and $s_2(v)$ (with u, v scalars, and s_1, s_2 belonging to the (x,z) -plane) to define these surfaces. Between the two solid surfaces, there is the fluid-fluid system, outside a solid, as shown in Fig. 3.
- We set the initial positions of the free points P_i ($i = 1, \dots, N$) in the space between $s_1(u)$ and $s_2(v)$, and of the extreme points C_1 and C_2 on the surface of the solid 1 and solid 2, respectively. The interface is given by the set of segments linking any two consecutive points. By definition, P_{i+1} is consecutive to P_i , P_1 to C_1 and C_2 to P_N . These initial positions define also the volume of the two fluids.
- The annealing temperature T , introduced in Eq. (29), is set to its initial value T_0 .
- A point is randomly selected.

If the selected point is a free point, say P_i , it is moved in the (x,z) -plane by the displacement (δ_x, δ_z) to its new position P'_i (see Fig. 13(a)), where δ_x and δ_z are randomly selected within $[-\delta_{max}/2, \delta_{max}/2]$. If the segment $P_i P_{i+1}$

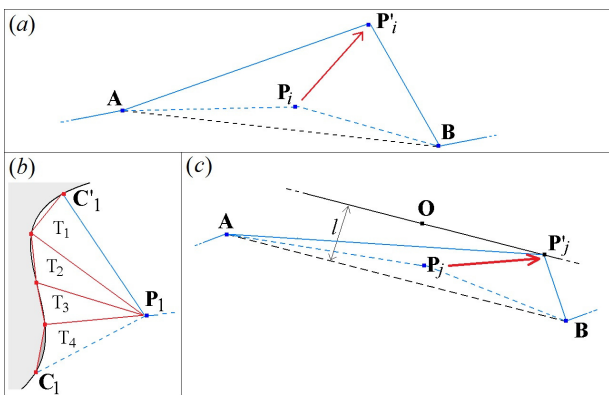


FIG. 13. (a): Movement of a free point; (b): decomposition in triangles of the area between s_1 , C'_1P_1 , and C_1P_1 ; (c): free point movement to generate the desired variation in the volume of fluid 2.

crosses a solid surface or the interface, then the move is rejected and the program goes to step “(l).”

If the selected point is C_k ($k = 1, 2$), it is moved along s_k (in one of the two possible directions, randomly chosen) until it covers a path of length δ , where δ is randomly chosen within $[0, \delta_{max}/2]$. Given its new position C'_k , if the segment C'_1P_1 or $P_N C'_2$ crosses the interface, then the move is rejected and the program goes to step “(l).”

- (e) The variation $\delta\varepsilon_g$ of the gravitational term of ε due to the point move in step “(d)” is calculated.

If the point moved is a free point, say P_i , then: $\delta\varepsilon_g = a\hat{G}(\mathbf{AP}_i\mathbf{B}) + b\hat{G}(\mathbf{AP}'_i\mathbf{B})$, where \mathbf{A} and \mathbf{B} are the two closest neighbors of P_i on the interface, and $\hat{G}(\mathbf{ABC})$ is the gravitational energy of the triangle \mathbf{ABC} , scaled with ξ_y and γ , and it is computed as

$$\hat{G}(\mathbf{ABC}) = \frac{\hat{A}(\mathbf{ABC})}{\ell^2} \frac{(\mathbf{A} + \mathbf{B} + \mathbf{C}) \cdot \mathbf{z}}{3}, \quad (\text{A1})$$

where $\hat{A}(\mathbf{ABC})$ is the area of the triangle \mathbf{ABC} . Then, $a, b = \pm 1$, where (see Fig. 13(a)) b is equal to the sign of $[(\mathbf{A} - \mathbf{B}) \times (\mathbf{A} - \mathbf{P}'_i)] \cdot \hat{\mathbf{y}}$, with $\hat{\mathbf{y}}$ the normal in the y direction (i.e., pointing out of the paper). Then, $a = b$ if the segment $\mathbf{P}_i\mathbf{P}'_i$ intersects the line passing through the segment \mathbf{AB} , otherwise $a = -b$.

If the point moved is C_k ($k = 1, 2$), then the area between s_1 , C'_1P_1 and C_1P_1 (or s_2 , C'_2P_N and C_2P_N) is decomposed into a certain number of triangles T_f (see Fig. 13(b)), and $\delta\varepsilon_g = \pm \sum_f \hat{G}(T_f)$, with the sign “ \pm ” positive if fluid 2 is gaining volume (moving C_k in C'_k), otherwise negative.

- (f) The interface surface variation δS due to the point move in step “(d)” is calculated as the length variation of the segments forming the interface (and it is negative if the total length of the segments was decreased, positive otherwise).
- (g) If the point moved in “(d)” is C_k ($k = 1, 2$), then the variation in the k th solid surface wet by fluid 2 is computed as $\delta W_2(k) = \pm \left| \int_{C'_k}^{C_k} s_k(u) du \right|$, with “ \pm ” positive if fluid 2 is gaining volume (moving C_k in C'_k), otherwise negative. If the point moved in “(d)” is a free point, then $\delta W_2(k) = 0$.
- (h) The volume variation δV of the fluid 2 is calculated. If the point moved in “(d)” was a free point, say P_i , then,

$\delta V = a\hat{A}(\mathbf{AP}_i\mathbf{B}) + b\hat{A}(\mathbf{AP}'_i\mathbf{B})$, where \mathbf{A} and \mathbf{B} are the two closest neighbors of P_i on the grid, $\hat{A}(\mathbf{ABC})$ is the area of the triangle \mathbf{ABC} , and $a, b = \pm 1$. The signs of a and b are computed as described in step “(e).” If the point moved in “(d)” was C_k ($k = 1, 2$), then the area between s_1, C'_1P_1 and C_1P_1 (or s_2, C'_2P_N and C_2P_N) is decomposed in a certain number of triangles T_f (see Fig. 13(b)) and $\delta V = \pm \sum_f \hat{A}(T_f)$, with “ \pm ” positive if fluid 2 is gaining volume (moving C_k in C'_k), otherwise negative.

- (i) Another point is randomly selected and it is moved to compensate the volume variation calculated in step “(h).” Just for simplicity, in this step, we choose only free points. Say P_j is the selected point. First, the point \mathbf{O} at a distance $l \equiv 2|\delta\tilde{V}|/|\mathbf{AB}|$ from the segment \mathbf{AB} is calculated (see Fig. 13(c)), where \mathbf{A} and \mathbf{B} are the two closest neighbors of P_j , $\delta\tilde{V} = \delta V + \mathbf{AP}_j \times \mathbf{AB}/2$. The side of \mathbf{O} with respect to the segment \mathbf{AB} is such that $\mathbf{AO} \times \mathbf{AB}$ has the same sign as $\delta\tilde{V}$. Then, the new position P'_j is found moving \mathbf{O} by a random amount $\delta \in [0, \delta_{max}/2]$ in one of the two directions parallel to \mathbf{AB} (which direction is randomly chosen). In this way, the total volume variation due to the moves in this step and in step “(d)” is zero. If the segment $\mathbf{P}'_j\mathbf{P}_j$ crosses a solid surface or the interface, then the move is forbidden and the program goes to the step “(l).”
- (j) The variations due to the move in step “(i)” in the gravitational part of ε and in the fluid-fluid surface (respectively, $\delta\varepsilon'_g$ and $\delta S'$) are computed as described in the steps “(e)” and “(f).” Then, the total variation in the functional ε due to the moves in the steps “(d)” and “(i)” is calculated as $\delta\varepsilon = \delta\varepsilon_g + \delta\varepsilon'_g + \delta S + \delta S' - \cos\theta_k \delta W_2(k)$, where θ_k is the contact angle of the k th solid surface.
- (k) With a probability \mathcal{P} (see Eq. (29)) the new configuration of the system is accepted, where $\Delta E = \gamma\xi_y \delta\varepsilon$, otherwise the two points moved, respectively, in step “(d)” and “(i)” return to their previous positions.
- (l) The program returns to step “(d).” Every M times this step is performed, T is decreased by an amount δT . If $T \leq 0$, then the simulation ends.

To efficiently run this algorithm and obtain the correct solution, it is necessary to choose properly all the simulation parameters involved ($T, T_0, N, \delta_{max}, M$, and δT). In principle, a good choice of this set can be found only heuristically. However, this problem, which is intrinsic to the method, needs to be faced only in a first stage. Then, the method can be applied systematically to a certain class of problems by keeping the same structure of parameters, with at most some minor adjustments. In Table II, we report all the simulation parameter values that we used for the results of Sec. IV.

This algorithm can be adapted to simulate a system where two or more one-dimensional grids of points are necessary to represent the interface (like in Sec. IV C). The necessary modifications are in step “(b),” defining all the solid surfaces, grids of points, and two constrained points for each grid, and in the step “(i),” choosing the free point randomly from every grid, to allow the exchange of volume between the regions below the different grids.

For the results of Sec. IV C (Fig. 8), we need the total energy $E = \varepsilon\gamma\xi_y$ (Eqs. (27)-(32)) of the final solution. We

TABLE II. Simulation parameters used in the various results shown in Sec. IV. δ_{max} is set to 0.5ℓ in all the simulations. About Fig. 8, N is referred to each one of the three grids of points. Each simulation was performed on an ordinary office PC and required few minutes to be completed.

Fig.	N	$\frac{k_B}{\gamma \ell^2} T_0$	$\frac{k_B}{\gamma \ell^2} \delta T$	M
4,6,7(b)	28	10^{-5}	10^{-7}	10^5
5	several	10^{-5}	10^{-7}	10^5
7(a)	28	0.01	10^{-4} if $T > 10^{-4}$, otherwise $5 \cdot 10^{-7}$	$2 \cdot 10^5$
8	13	0.11	10^{-4} if $T > 10^{-4}$, otherwise 10^{-7}	$3 \cdot 10^5$
10,11(a)	48	0.01	10^{-4} if $T > 10^{-4}$, otherwise $5 \cdot 10^{-7}$	$2 \cdot 10^5$
11(b)	38	0.01	10^{-4} if $T > 10^{-4}$, otherwise $5 \cdot 10^{-7}$	$2 \cdot 10^5$

calculate this using

$$\varepsilon = \varepsilon_g + S - \sum_k W_2(k) \cos \theta_k, \quad (\text{A2})$$

where S , $W_2(k)$, and ε_g , respectively, are the fluid-fluid surface, the k th solid-fluid 2 surface, and the gravitational part of ε (all referred to the final solution). They are computed updating their initial values as $S + \delta S + \delta S'$, $W_2(k) + \delta W_2(k)$, and $\varepsilon_g + \delta \varepsilon_g + \delta \varepsilon'_g$ in step “(k)” every time a new configuration is accepted.

To get the results of Sec. IV D about the pendant droplets (Fig. 11), the algorithm is modified to minimize Eq. (34) instead of Eq. (27). This is done simply by changing the signs of $\delta \varepsilon_g$ and $\delta \varepsilon'_g$ in step “(j)”.

¹E. Dickinson, *Trends Food Sci. Technol.* **24**, 4 (2012).

²S. Sacanna, W. K. Kegel, and A. P. Philipse, *Phys. Rev. Lett.* **98**, 158301 (2007).

³M. G. Basavaraj, G. G. Fuller, J. Fransaer, and J. Vermant, *Langmuir* **22**, 6605 (2006).

⁴M. G. Basavaraj, S. Vandebril, J. Fransaer, and J. Vermant, *Soft Matter* **5**, 1717 (2009).

⁵D. M. Andala, S. H. R. Shin, H. Lee, and K. J. M. Bishop, *ACS Nano* **6**, 1044 (2012).

⁶A. Dominguez, M. Oettel, and S. Dietrich, *Phys. Rev. E* **82**, 011402 (2010).

⁷B. J. Park and E. M. Furst, *Soft Matter* **7**, 7676 (2011).

⁸B. J. Park, T. Brugarolas, and D. Lee, *Soft Matter* **7**, 6413 (2011).

⁹P. J. Yunker, T. Still, M. A. Lohr, and A. G. Yodh, *Nature* **476**, 308 (2011).

¹⁰L. Botto, L. Yao, R. L. Leheny, and K. J. Stebe, *Soft Matter* **8**, 4971 (2012).

¹¹L. Botto, E. P. Lewandowski, M. Cavallaro, and K. J. Stebe, *Soft Matter* **8**, 9957 (2012).

¹²B. J. Park, C. Choi, S. Kang, E. Tettey, C. Lee, and D. Lee, *Soft Matter* **9**, 3383 (2013).

¹³R. McGorty, J. Fung, D. Kaz, and V. N. Manoharan, *Mater. Today* **13**, 34 (2010).

¹⁴Z. Niu, J. He, T. P. Russell, and Q. Wang, *Angew. Chem. Int. Ed.* **49**, 10052 (2010).

¹⁵E. M. Furst, *PNAS* **108**, 20853 (2011).

¹⁶V. Garbin, J. C. Crocker, and K. J. Stebe, *J. Colloid Interface Sci.* **387**, 1 (2012).

¹⁷E. P. Lewandowski, J. A. Bernate, P. C. Searson, and K. J. Stebe, *Langmuir* **24**, 9302 (2008).

¹⁸M. Cavallaro, L. Botto, E. P. Lewandowski, M. Wang, and K. J. Stebe, *PNAS* **108**, 20923 (2011).

¹⁹D. Ershov, J. Sprakler, J. Appel, M. A. Cohen Stuart, and J. van der Gucht, *PNAS* **110**, 9220 (2013).

²⁰B. Madivala, J. Fransaer, and J. Vermant, *Langmuir* **25**, 2718 (2009).

²¹E. P. Lewandowski, J. A. Bernate, A. Tseng, P. C. Searson, and K. J. Stebe, *Soft Matter* **5**, 886 (2009).

²²W. Qi, J. de Graaf, F. Qiao, S. Marras, L. Manna, and M. Dijkstra, *Nano Lett.* **12**, 5299 (2012).

²³H. Evers, B. Goris, S. Bals, J. Casavola, M. de Graaf, R. van Roij, M. Dijkstra, and D. Vanmaekelbergh, *Nano Lett.* **13**, 2317 (2013).

²⁴T. M. Ruhland, A. H. Gröschel, A. Walther, and A. H. E. Müller, *Langmuir* **27**, 9807 (2011).

²⁵A. D. Law, M. Auriol, D. Smith, T. S. Horozov, and D. M. A. Buzzia, *Phys. Rev. Lett.* **110**, 138301 (2013).

²⁶L. N. Arnaudov, O. J. Cayre, M. A. Cohen Stuart, S. D. Stoyanov, and V. N. Paunov, *Phys. Chem. Chem. Phys.* **12**, 328 (2010).

²⁷L. Isa, E. Amstad, K. Schwenke, E. Del Gado, P. Ilg, M. Kröger, and E. Reimhult, *Soft Matter* **7**, 7663 (2011).

²⁸A. Kumar, B. J. Park, F. Tu, and D. Lee, *Soft Matter* **9**, 6604 (2013).

²⁹S. Coertjens, P. Moldenaers, J. Vermant, and L. Isa, *Langmuir* **30**, 4289 (2014).

³⁰A. Stocco, G. Su, M. Nobili, M. In, and D. Wang, *Soft Matter* **10**, 6999 (2014).

³¹J. de Graaf, M. Dijkstra, and R. van Roij, *Phys. Rev. E* **80**, 051405 (2009).

³²J. de Graaf, M. Dijkstra, and R. van Roij, *J. Chem. Phys.* **132**, 164902 (2010).

³³B. J. Park and D. Lee, *ACS Nano* **6**, 782 (2012).

³⁴B. J. Park and D. Lee, *Soft Matter* **8**, 7690 (2012).

³⁵W. van der Stam, A. Gantapara, Q. A. Akkerman, G. Soligno, J. M. Meeldijk, R. van Roij, M. Dijkstra, and C. de Mello Donega, *Nano Lett.* **14**, 1032 (2014).

³⁶B. Peng, G. Soligno, M. Kamp, B. de Nijs, J. de Graaf, M. Dijkstra, R. van Roij, A. van Blaaderen, and A. Imhof, *Soft Matter* **10**, 9644 (2014).

³⁷L. D. Landau and E. M. Lifshitz, *Statistical Physics - Part I*, 3rd revised and enlarged edition (Pergamon Press, 1980), pp. 531–533.

³⁸R. Defay and I. Prigogine, *Surface Tension and Adsorption* (Longmans, 1966), pp. 6–7.

³⁹C. Pozrikidis, *Introduction to Theoretical and Computational Fluid Dynamics* (Oxford University Press, 1997), pp. 159–160.

⁴⁰M. J. Smith, *Am. J. Phys.* **38**, 1153 (1970).

⁴¹P. Roura, *Am. J. Phys.* **73**, 1139 (2005).

⁴²K. A. Brakke, *Exp. Math.* **1**, 141 (1992).

⁴³Y. Tsori, *Langmuir* **22**, 8860 (2006).

⁴⁴K. D. Danov and P. A. Kralchevsky, *Adv. Colloid Interface Sci.* **154**, 91 (2010).

⁴⁵C. Zeng, F. Brau, B. Davidovitch, and A. D. Dinsmore, *Soft Matter* **8**, 8582 (2012).

⁴⁶H. Cooray, P. Cicuta, and D. Vella, *J. Phys.: Condens. Matter* **24**, 284104 (2012).

⁴⁷D. B. Quinn, J. Feng, and H. A. Stone, *Langmuir* **29**, 1427 (2013).

⁴⁸C. Blanc, D. Fedorenko, M. Gross, M. In, M. Abkarian, M. A. Gharbi, J. Fournier, P. Galatola, and M. Nobili, *Phys. Rev. Lett.* **111**, 058302 (2013).

⁴⁹H. Rezvantalab and S. Shojaei-Zadeh, *Soft Matter* **9**, 3640 (2013).

⁵⁰S. Razavi, J. Koplik, and I. Kretzschmar, *Soft Matter* **9**, 4585 (2013).

⁵¹S. Razavi, I. Kretzschmar, J. Koplik, and C. E. Colosqui, *J. Chem. Phys.* **140**, 014904 (2014).

⁵²J. Bleibel, A. Dominguez, M. Oettel, and S. Dietrich, *Soft Matter* **10**, 4091 (2014).

⁵³G. Whyman and E. Bormashenko, *J. Colloid Interface Sci.* **331**, 174 (2009).

⁵⁴A. K. Das and P. K. Das, *Chem. Eng. Sci.* **65**, 4027 (2010).

⁵⁵J. Guzowski, M. Tasinkeyevych, and S. Dietrich, *Soft Matter* **7**, 4189 (2011).

⁵⁶V. A. Lubarda, *Langmuir* **27**, 10705 (2011).

⁵⁷V. A. Lubarda, *Soft Matter* **8**, 10288 (2012).

⁵⁸T. Cheng and Y. U. Wang, *Langmuir* **28**, 2696 (2012).

⁵⁹T. Cheng and Y. U. Wang, *J. Colloid Interface Sci.* **402**, 267 (2013).

⁶⁰L. D. G. Sigalotti, J. Troconis, E. Sira, F. Peña Polo, and J. Klapp, *Phys. Rev. E* **90**, 013021 (2014).

⁶¹J. H. Weijis, J. H. Snoeijer, and B. Andreotti, *Phys. Rev. E* **89**, 042408 (2014).

- ⁶²M. Rivetti and A. Antkowiak, *Soft Matter* **9**, 6226 (2013).
- ⁶³L. A. Lubbers, J. H. Weijts, L. Botto, S. Das, B. Andreotti, and J. H. Snoeijer, *J. Fluid Mech.* **747**, R1 (2014).
- ⁶⁴J. C. F. Gauss, *Principia Generalia Theoriae Figurae Fluidorum* (Dieterichs, 1830).
- ⁶⁵S. Kirkpatrick, C. D. Gelatt, and M. P. Vecchi, *Science* **220**, 671 (1983).
- ⁶⁶L. D. Landau and E. M. Lifshitz, *Fluid Mechanics*, 2nd english revised edition (Pergamon Press, 1987), pp. 242–243.
- ⁶⁷P. de Gennes, F. Brochard-Wyart, and D. Qéré, *Capillarity and Wetting Phenomena* (Springer, 2004), p. 46.
- ⁶⁸M. Sbragaglia, L. Biferale, G. Amati, S. Varagnolo, D. Ferraro, G. Mistura, and M. Pierno, *Phys. Rev. E* **89**, 012406 (2014).
- ⁶⁹M. Rauscher and S. Dietrich, *Soft Matter* **5**, 2997 (2009).
- ⁷⁰R. Daly, J. E. Sader, and J. J. Boland, *Langmuir* **28**, 13218 (2012).
- ⁷¹M. J. Neeson, R. F. Tabor, F. Grieser, R. R. Dagastine, and D. Y. C. Chan, *Soft Matter* **8**, 11042 (2012).